Title

Micro-patterned graphene-based sensing skins for human physiological monitoring

Journal

Nanotechnology, 29(10)

ISSN

0957-4484

Authors

Wang, Long
Loh, Kenneth J
Chiang, Wei-Hung
et al.

Publication Date

2018-03-09

DOI

10.1088/1361-6528/aaa709

Peer reviewed

Micro-patterned graphene-based sensing skins for human physiological monitoring

Long Wang[1], Kenneth J. Loh[1,*], Wei-Hung Chiang[2,+], and Kausik Manna[2]
[1]Department of Structural Engineering, University of California-San Diego, La Jolla, CA, 92093-0085, USA
[2]Department of Chemical Engineering, National Taiwan University of Science & Technology, Taipei 106, Taiwan

[*]Co-corresponding author e-mail: kenloh@ucsd.edu
[+]Co-corresponding author e-mail: whchiang@mail.ntust.edu.tw

Abstract. Ultrathin, flexible, conformal, and skin-like electronic transducers are emerging as promising candidates for noninvasive and nonintrusive human health monitoring. In this work, a wearable sensing membrane is developed by patterning a graphene-based solution onto ultrathin medical tapes, which can then be attached to the skin for monitoring human physiological parameters and physical activity. Here, the sensor is validated for monitoring finger bending/movements and for recognizing hand motion patterns, thereby demonstrating its future potential for evaluating athletic performance, physical therapy, and designing next-generation human-machine interfaces. Furthermore, this study also quantifies the sensor′s ability to monitor eye blinking and radial pulse in real-time, which can find broader applications for the healthcare sector. Overall, the printed graphene-based sensing skin is highly conformable, flexible, lightweight, nonintrusive, mechanically robust, and is characterized by high strain sensitivity.
Keywords: human sensing, graphene, patterning, physiological monitoring, sensing skin

1. Introduction

A plethora of nanostructured materials-based wearable sensors have been developed in recent years, where they possess tremendous advantages (e.g., greater flexibility, sensitivity, and multi-functionality) as compared to conventional bulky electronics-based transducers [1-3]. Among the various sensing modalities explored, strain is an essential parameter that can provide rich information regarding human behavior and for physiological assessment. High-performance strain sensors of various configurations (including thin films [2, 4-7], yarn fibers [8, 9], and sponges [10], among others) leverage the extraordinary mechanical and electrical properties of nanomaterials (such as carbon nanotubes (CNT) [2, 11, 12], metallic nanowires (NW) [4, 5], and graphene [8, 12-16]) to enhance their performance. When wearable sensors are directly applied onto human skin using tapes [2, 8-10], accurate measurements can only be obtained if the sensor conforms to and exhibits similar compliance with the skin [2, 8, 10, 13]. On the other hand, patterning the strain sensing elements allows spatially selective sensing, heterogeneous designs for multi-scale motions [17], and multi-directional strain measurements [14]. Examples include photolithography-based strain sensing silicon (Si) traces [17], chemical vapor deposition (CVD)-grown CNT or graphene patterns [2, 14, 15], screen printed nanocomposites [1, 18], and inkjet-printed electronics [19-21]. However, autonomous patterning and cost-effective manufacturing are still major challenges that have limited the transition of this emerging technology to the marketplace.

In this study, a micro-patterned, graphene-based, skin-like, wearable sensor was developed for monitoring human activity and physiological parameters. The sensing element was fabricated by printing dispersed graphene solutions to form strategically designed functional geometrical patterns (such as strain rosettes) directly onto ultrathin medical tape, thereby simplifying fabrication and eliminating the need for masks, molds, or sacrificial layers. The printed graphene sensor (PGS)

exhibited superior strain sensing performance, including high signal-to-noise ratio (SNR), high gage factor (GF) (i.e., 21 within 10 % strain and 142 within 20 % strain), and consistent repeatability (through 1000 cycles of load tests). In addition, the PGS is ultra-lightweight (3.9 mg cm^{-2}), directly attachable to the skin, highly conformable, and mechanically robust (where it remains intact after 100 cycles of vigorous skin deformations). The potential applications of the PGS were demonstrated by detecting and recognizing hand motions, as well as monitoring eye blinking and radial pulse.

2. Experimental details

2.1. Materials

Graphite (-325 mesh, 99.995% pure) microcrystalline powders and N-methylpyrrolidinone (NMP, 99% extra pure) were from Alfa Aesar and ACROS ORGANICS, respectively. Polyoxyethylene (40) nonylphenyl ether (IGEPAL® CO890, average M_n ~ 1982, branched) was purchased from Sigma–Aldrich. Ultrathin (8 μm) medical tape was provided by Nitoms (XTRATA® Perme-Roll AIRTM). Conductive thread and conductive silver paint were purchased from Adafruit and Ted Pella, respectively. Dragon Skin® FX-Pro was from Smooth-On.

2.2. Synthesis and characterization of graphene nanosheet (GNS)

Figure 1 shows a schematic illustration of the preparation of the GNS and the fabrication process of the PGS. GNS was synthesized from bulk graphite via water-assisted liquid-phase exfoliation (WALPE) in a co-solvent of NMP and deionized water (8:2 mixing ratio) (step i). WALPE synthesis was used for its low-cost, efficient, high-yield, and environmental friendly attributes [22]. In addition, the WALPE is promising to produce few-layer liquid-phase exfoliated graphene nanosheets (LPEGNS) with relatively intact nanostructures as compared to conventional reduced graphene oxide (RGO) [23].

Here, 50 mg of each material was measured and placed in 14 mL centrifuge tubes with an initial concentration 5 mg mL^{-1} for exfoliation. The same 14 mL centrifuge tubes were used throughout the experiments to avoid material loss due to transfer. The materials were bath sonicated for 6 h (Elma sonic P60H) at a fixed nominal power and frequency of 100 W and 37 kHz, respectively. The positions of each sample tube were interchanged every 30 min to subject the mixtures to uniform power distribution. The water of the bath sonicator was replaced with cold water every 30 min to minimize temperature increase during sonication; temperature was maintained between 27~37 °C. Sample dispersions were left overnight after sonication, followed by centrifugation at 3000 rpm for 30 min using a Hettich EBA20 centrifuge. The top 75% of the colloidal supernatant was first collected. Then, the supernatant was kept undisturbed for 24 h for further precipitation, if any, and the upper 67% portion of the colloidal supernatant was used for characterization. Every experiment was repeated for five times to obtain statistically representative results and to account for experimental error.

Ex situ characterization of the as-produced GNS was performed by transmission electron microscopy (TEM) and micro-Raman spectroscopy. Cold-field emission Cs-corrected TEM (JEOL ARM-200F) with 200 kV accelerating voltage was used. Carbon-coated copper grids (400 mesh) were

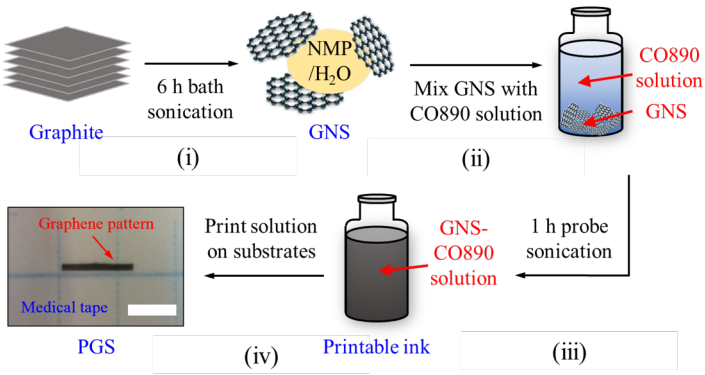

Figure 1. Schematic illustration for (i) GNS synthesis, (ii and iii) printable ink preparation, and (iv) micro-patterning the ink on the substrates. Scale bar, 10 mm.

used for TEM sample preparation. Raman scattering was performed at room temperature with a JASCO 5100 spectrometer (λ = 533 nm). The thin films for Raman analysis were prepared on silicon wafers and dried in a hot air oven at 60 °C.

2.3. Fabrication of the PGS

To obtain printable GNS-based ink, 0.5 wt% CO890 was first dissolved in deionized (DI) water by bath sonication (Fisher® Scientific) for 1.5 h. Second, a mixture of 1 mg mL^{-1} of as-synthesized GNS and 0.5 wt% CO890 aqueous solution was then subjected to 1 h of high-energy probe sonication (3 mm tip, 150 W, 22 kHz), as is shown in figure 1 (step ii and iii). Here, an aqueous solution was used instead of organic solvents to maintain compatibility with the printing substrates. Then, a Microplotter® (SonoPlot) was employed for patterning the dispersed GNS-CO890 solution onto the ultrathin medical tape at room temperature, forming pre-designed, 2D geometrical patterns during fabrication (step iii) [24]. The printing resolution was ~ 60 μm. It should be noted that the Microplotter® can fabricate complex geometries, but, in this study, the sensing elements were only rectangular for simplicity sakes. Then, the as-printed patterns were air-dried at room temperature. Unlike traditional patterning techniques (e.g., photolithography, soft lithography, and screen printing), patterned PGS was fabricated at a low temperature and without the use of masks and molds. In particular, each GNS-based sensing element was pre-designed as 12 mm × 1 mm-thin rectangles using AutoCAD (Autodesk). The designed patterns could be printed multiple times onto the previously deposited layer, where each pass of the Microplotter® formed one layer of the multi-layered PGS. Finally, the electrodes were established on the printed patterns by drying conductive silver paint over the sensing element and electrically conductive threads.

2.4. PGS microstructures characterization

The microstructure of the printed graphene patterns was investigated using micro-Raman spectroscopy and scanning electron microscope (SEM). Here, specimens were fabricated by printing 4- and 14-layer of GNS sensing elements onto polyethylene terephthalate (PET) substrates. It should be noted that, instead of using medical tape, the rigidity and transparency of the PET substrates made it easier to perform microscopy. In particular, micro-Raman scattering studies were performed at room temperature with a JASCO 5100 spectrometer (λ = 533 nm). The Raman spectra were recorded using 10 random spots on the specimens. The effect of laser heating was avoided by maintaining the laser beam intensity at 0.1 mW. In addition, SEM (JEOL JSM-6500F) was used to qualitatively observe the surface morphologies of the printed graphene patterns. The accelerating voltages were set to between 10 to 15 kV.

2.5. Mechanical Tests

The mechanical properties of the pristine medical tapes as well as the PGS were characterized by conducting uniaxial tensile tests using a Test Resources 100R electromechanical load frame. The main goal was to study whether the printed GNS patterns affected the mechanical properties of the substrate. Here, the specimens were stretched at a loading rate of 20 % min^{-1}. Then, the corresponding stress-strain curves were obtained by considering their dimensions and applied force, which was recorded during load testing.

2.6. Strain sensing tests

The test coupons were prepared by transferring the PGS to the test phantom, so as to mimic a simplified PGS-skin structure. The phantom or surrogate skin was fabricated by spin coating (1200 rpm, 30 s, spin coater model WS-650MZ-23NPPB, Laurell Technologies) stretchable and low modulus (~ 190 kPa) Dragon Skin® (a 1:1 mixture of parts A and B). After being air-dried at room temperature, the phantom skin was removed from the glass substrates. The resulting phantom had an average thickness of ~ 90 μm, which was cut to 50 mm × 28 mm individual specimens. Then, the PGS was attached onto the phantom skin to form the test specimens. Figures 2a and 2b illustrate an explosion-view of the laminated test coupon structure and a photograph of an assembled specimen. The inset of figure 2b shows an assembled specimen that collapsed under its own self-weight, further indicating the flexibility of the device.

Before conducting load tests, the nominal resistance of the PGS was first characterized. Here, PGS of different numbers of layers (i.e., 4, 8, 12, 18, and 24 layers) were fabricated. The resistance time

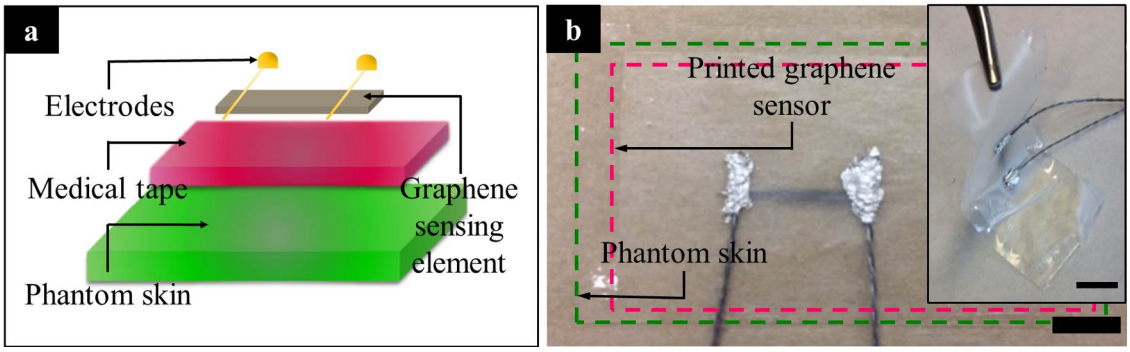

Figure 2. (a) An explosion-view of the test coupon structure. (b) An assembled coupon for strain sensing tests. The left inset illustrates a magnified-view of the test coupon structure. The inset illustrates the flexible configuration of the device. All scale bars, 10 mm.

histories of the specimens were recorded using a DMM when they remained un-deformed and at room temperature. Then, an electromechanical load frame (150R, TestResources) was employed for applying tensile cyclic loads to the specimens. During the load tests, the resistance time history of the PGS specimen was measured using digital multimeters (DMM) (34465A, Keysight Technologies) interfaced to a Keysight BenchVue program for data acquisition and storage. Here, multiple tensile cyclic strain patterns to different peak strains (i.e., 0.5%, 1%, 2%, 4%, 8%, 10%, and 20%) were applied at a constant load frequency of 0.5 Hz. In addition, the long-term strain sensing response was investigated by subjecting the PGS specimen to 2000-cycle loads with a peak strain of 1% at 0.5 Hz loading frequency.

2.7. Human motion and physiological performance monitoring

2.7.1. PGS-skin compliance characterization. For the sensing membranes to be directly adhered onto human skin, they need to be highly conformable so as to establish effective contact, but skin is well known to contain roughness features that span multiple length scales [25]. In addition, the sensor needs to deform together with skin to guarantee reliable strain transfer. Currently, different sensing skin platforms have been reported, such as tacky poly(dimethylsiloxane) (PDMS) thin films [3, 26] and PDMS-based micro-fiber arrays [27, 28]. In this study, highly flexible, ultrathin, lightweight, and breathable medical tape was employed as substrate for the PGS sensing element, which can then be directly attached onto skin. To characterize the mechanical robustness of the PGS-skin attachment, the PGS was adhered onto a subject's arm and was subjected to various deformations. In addition, the PGS was implemented on a human subject for 2 h, during which the subject performed daily activities.

2.7.2. Hand motion monitoring. To demonstrate the PGS' potential for monitoring various human activities in real-time, a series of experiments were conducted. Here, the PGS specimens tested consisted of 4 printed layers, mainly to leverage the superior sensing properties of the 4-layer PGS for accurate measurements. First, the PGS was attached to a subject's index finger for detecting finger movements. Figure 3a (i) and (ii) depict the top and side views of the experimental setup, respectively, where the graphene sensing element was aligned with the longitudinal direction of the index finger. During the tests, the finger repeatedly bent to different pre-calibrated angles (figures 3a (iii) ~ (vi)) in a random manner so as to prevent biasing the results if bending was monotonically increased. In the meantime, the PGS' resistance time history was recorded.

Furthermore, it should be noted that, in real-world applications, wearable sensors can be subjected to sophisticated, multi-axis strains (including shear). In order to develop wearable sensors that can characterize complex skin deformations and infer corresponding muscle contractions, simultaneous strain measurements in different directions are needed. Therefore, by further leveraging the advantages of printing technology, PGS was patterned to form a rosette. The sensing elements include three GNS strips oriented in three different directions (i.e., S_a, S_b, and S_c), as shown in the inset of figure 3b (i). Here, to validate multi-directional strain sensing, the PGS rosette was adhered onto the back of a subject's hand (see figure 3b (i)) for distinguishing different hand motion patterns. Figure 3b (ii) shows

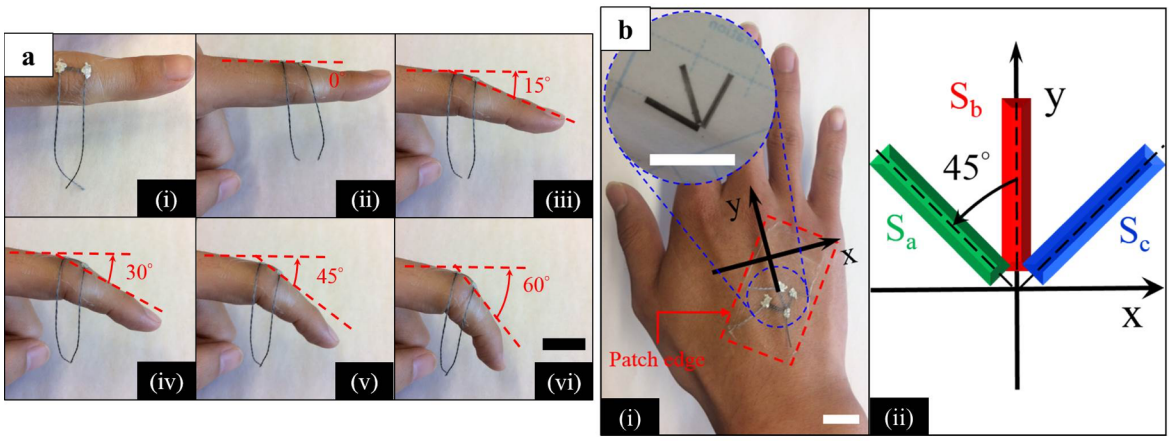

Figure 3. (a) (i) Top view of a PGS mounted onto the index finger. (ii-vi) Side views of the finger bent to different angles (i.e., 0°, 15°, 30°, 45°, and 60°, respectively). (b) (i) Top view of a PGS rosette attached to the back of the hand. The inset shows the PGS rosette before mounting. (ii) A schematic of the orientation of the PGS rosette.

a schematic illustration of the orientation of the PGS rosette with respect to a predefined Cartesian coordinate system.

2.7.3. Human physiological performance monitoring. Besides sensing human motions, the PGS was also demonstrated for monitoring human physiological performance in real-time by measuring subtle motions of the body. First, the PGS was employed for detecting eye blinking. Eye movement and blinking are significant clinical parameters for behavior-based diagnosis of impaired consciousness (i.e., coma, vegetative state, and minimally conscious state (MCS)) for patients with brain damage [29]. On the other hand, as for patients with locked in syndrome (LIS) who have complete tetraplegia while preserving intact consciousness and eye movement and blinking, their communication solely depends on eye movement and blinking [30, 31]. In addition, the frequency and intensity of eye blinking can indicate human fatigue to some extent. Therefore, by monitoring eye blinking, the PGS is envisioned to facilitate high-fidelity diagnosis of consciousness, improve communications with LIS patients, and facilitate detection of fatigue. During the experiments, the PGS was vertically attached to the lateral canthus of a human subject, who blinked repeatedly.

Second, radial pulse is one of the most representative vital signals that is commonly measured in clinical practice to quantify human physiological performance (e.g., blood pressure, heart rate, and vascular stiffness) [32]. Moreover, radial pulse wave monitoring also facilitates early diagnosis of cardiovascular diseases. Here, the PGS' potential for monitoring pulsation was explored by attaching the PGS onto the surface of the skin close to the radial artery of a human subject's (a 25-year-old male)

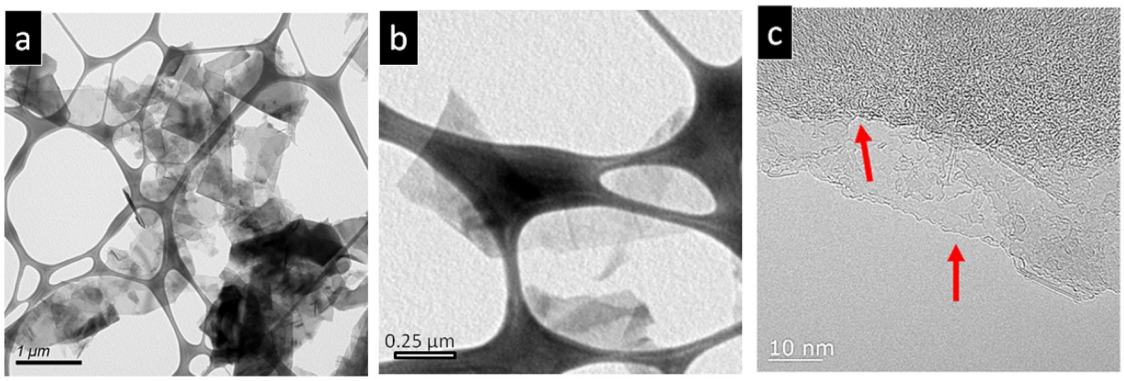

Figure 4. (a – c) TEM images of different magnifications for the GNS synthesized by the WALPE method. The red arrows in (c) indicate the distinct edges of the few-layer GNS.

wrist. The PGS was used to measure pulse signal when the subject was at rest and after rigorous exercise for 40 s.

3. Results and discussion

3.1. Characterization of the GNS

Figure 4 shows the TEM images of different magnifications of the as-synthesized GNS. The red arrows in figure 4 (c) indicate the distinct layers of GNS, showing that they had few layers as well as relatively intact nanostructures. In addition, the Raman spectrum of the GNS is shown in figure 5. The impurities or defects in the graphene basal plane were quantified from the intensity ratio of D to G band (I_D/I_G). The low value of I_D/I_G (~ 0.60) and high 2D peak intensity of GNS indicated that the water-NMP co-solvent approach resulted in fewer defects in GNS during synthesis [22, 33, 34]. The WALPE method was capable of obtaining high-quality GNS due to the interactions between GNS and the co-solvent. In particular, the bulky $(NMP{\cdot}2H_2O)_n$ aggregates, formed due to water-NMP hetero-association, can generate inter-sheet repulsive forces and separate individual GNS with non-overlapping Leonard-Jones (L-J) potentials [22, 23]. Therefore, the WALPE method can preserve the unique properties of graphene, and is suitable for scale-up and enhancing bulk sensor performance.

3.2. PGS microstructures

Figure 6a shows the representative Raman spectra of the printed graphene sensing element. The result shows three typical peaks, namely, the D, G, and 2D bands at 1340, 1577, and 2692 cm^{-1}, respectively, which are consistent with previously reported Raman spectrum of LPEGNS [35, 36]. The increase in the dominance of GNS' featured peaks indicates that a denser graphene network was established as more ink was printed, which was further characterized using SEM, as is shown in figures 6b (i) and (iii). In addition, figures 6b (ii) and (iv) show the magnified view of the GNS network's 2D film-like surface morphology, which implies that graphene was efficiently dispersed and deposited without aggregation.

3.3. Strain sensing response

Figure 7 shows the average nominal resistance of the PGS fabricated using different numbers of printed layers. To render the GNS-based pattern electrically conductive, at least 4 printed layers were required. In addition, as more layers were deposited (i.e., incorporating more GNS), the printed trace became more conductive.

Figure 8a shows the stress-strain curves of the pristine medical tape and the PGS. It can be seen that printing the GNS-based patterns onto medical tape barely affected the mechanical properties of the pristine substrate. Figure 8b exhibits the un-deformed and deformed configurations of a specimen mounted in the load frame. In general, the printed GNS sensing element deformed conformably with the substrate without any visible delamination. Figure 8c illustrates a representative normalized change in resistance (R_n) time history response of a PGS-phantom skin when subjected to different applied

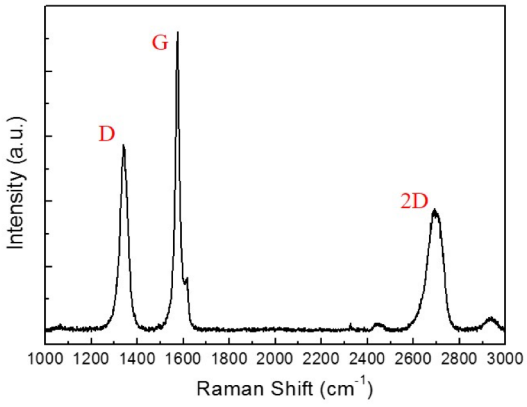

Figure 5. A representative Raman spectrum of the as-synthesized LPEGNS.

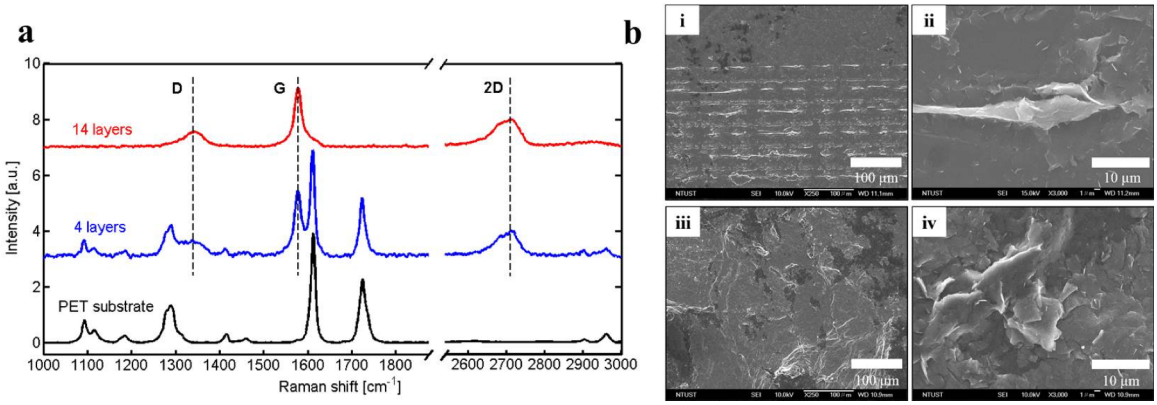

Figure 6. (a) Representative Raman spectra of the printed graphene network (i.e., 4- and 14-layer films) and the PET substrate. The intensity is of arbitrary unit for easy comparison. (b) SEM images of the surface morphologies of the (i) 4- and (iii) 14-layer GNS networks. (ii) and (iv) are magnified views of (i) and (iii), respectively.

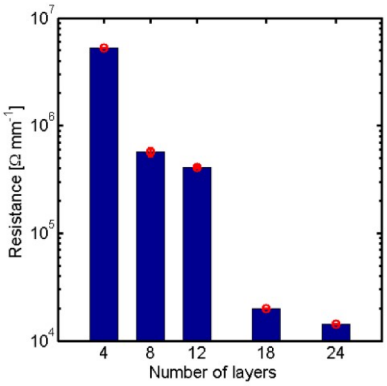

Figure 7. The nominal resistance of the PGS fabricated using different numbers of printed layers.

strain patterns. R_n is defined as $\Delta R/R_0$, where ΔR and R_0 are the change in resistance and unstrained or nominal resistance, respectively. The inset of figure 8c shows the specimen's response at low strains. The sensor's resistance increased in tandem with increasingly applied tensile strains, and the opposite was true during unloading, regardless of the magnitudes of applied peak strain. Its piezoresistive response is likely mainly due to deformation-induced changes in the conformation of the electrically conductive GNS network (i.e., contact resistance). Although the piezoresistivity of individual GNS was also reported [37, 38], in this study, GNS was assumed to be too rigid to be deformed by the interactions within the binder-free GNS network. Therefore, strain-induced changes in GNS-to-GNS junctions most likely dominated the piezoresistivity of the sensing element. In particular, it is hypothesized that GNS could undergo rigid-body motions within its compliant matrix as strain was applied to deform the substrate, thereby disrupting graphene-to-graphene junctions and the number of conductive pathways that exist within the film. However, the GNS network was able to restore back to its initial configuration upon strain release, thereby allowing resistance to decrease and return to its nominal resistance when strain was completely removed [39, 40].

Furthermore, to quantify strain sensing performance, GF, or strain sensitivity, of the PGS was calculated using:

$$GF = \frac{\Delta R_n}{\Delta \varepsilon} \tag{1}$$

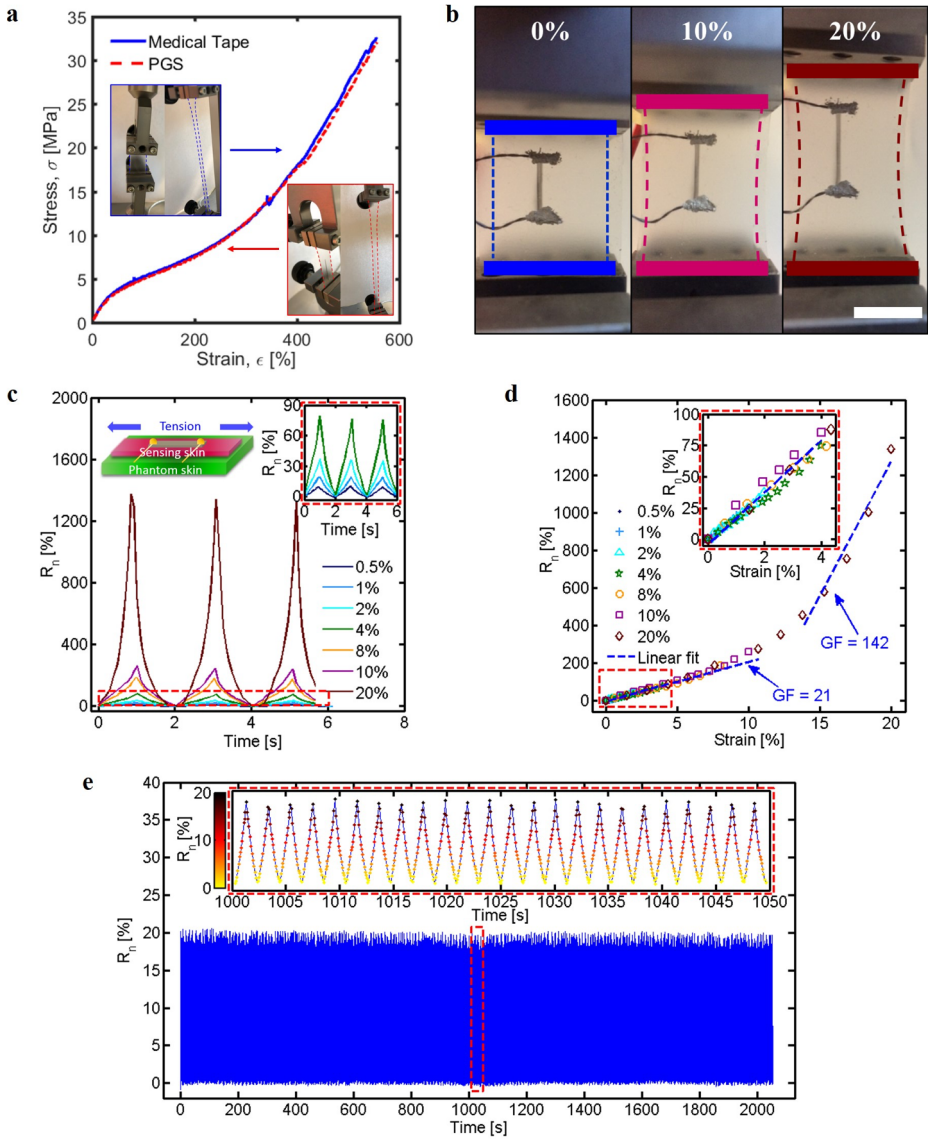

Figure 8. (a) The stress-strain curves of the medical tape and the PGS (printed onto medical tape). The insets show the medical tape (highlighted in blue) and the PGS samples (highlighted in red) mounted in the load frame during the tensile tests.(b) Images of a specimen subjected to 0 %, 10 %, and 20 % applied strains in the load frame. The dashed lines depict the edges of the PGS. Scale bar, 10 mm. (c) Representative R_n time histories of a specimen subjected to tensile cyclic strains of different peak magnitudes at a load frequency of 0.5 Hz. The inset confirms the sensor's linear response at low-strains. (d) The R_n data extracted from (c) plotted as a function of applied strains, and fitted by least-squares regression lines. The inset magnifies the region highlighted in the dashed box. (e) The R_n time history corresponding to cyclic load tests to 1 % peak strain at 0.5 Hz loading frequency. The inset shows the R_n data included in the 50 s time window.

where ΔR_n represents the change in R_n corresponding to the change in applied strain (ε). In figure 8c, R_n is plotted as a function of ε, and each set of raw data is then fitted with a least-square regression line. The slope of the best-fit line equates to GF. The inset of figure 8c shows a detailed view of the PGS' response when it was subjected to low levels of strains. The PGS exhibited ubiquitous linear strain sensing response and an average GF of 21 for applied strains up to ~ 10% (where the coefficient of determination or R^2 was 0.96), which is a preferable attribute. It can also be observed in figure 8d that the PGS was characterized by bilinear strain sensitivity when strained beyond 10%. GF was ~ 142 when applied strain was between 10% and 20%. The PGS developed in this study exhibited

significantly higher strain sensitivities than previously reported sensing skins, including silicon-based patterns (GF was ~5 [41] and ~1.6 [17]) and CVD-grown graphene patterns (GF was ~ 2.1 [15]). The observed nonlinearity of strain sensing response could be due to abrupt changes in the GNS network topology. To be specific, the microstructure of the GNS network might change from a "homogeneous network" to an "inhomogeneous network" when the applied strain increased beyond a certain threshold (i.e., ~ 10% in this case) [5, 42]. The nonlinear electromechanical performance was commonly reported for resistive strain sensors of high sensitivity but are relatively limited in stretch-ability [5, 14, 42, 43]. Future studies will focus on characterizing and improving the linearity of the sensing performance, especially under large strains. Here, as a proof of concept, it can be seen that the combination of high strain sensitivity, conformability, and mechanical robustness allows the PGS to not only be used for monitoring human motions but also subtle strains induced by pulsation. In addition, sensor durability was investigated by applying 1000 cycles of tensile strains, and a representative R_n time history plot is shown in figure 8e. The inset of figure 8e examines a magnified view of the response within a 50-s time window, which clearly shows the sensor's repeatable and stable electromechanical response. In addition, the repeatable response indicates that the PGS was mechanically intact throughout the entire load tests. Overall, the PGS is characterized by repeatable, reversible, and stable strain sensing performance and without noticeable fatigue degradation.

3.4. PGS-skin compliance

Figure 9a shows a PGS in its (i) un-deformed state and adhered onto the forearm of a subject; thereafter, the PGS was able to deform compliantly with different motions that induced (ii) compression, (iii) tension, and (iv) shear to the sensor. In addition, no damage to the PGS nor detachment occurred after it was repeatedly stretched and compressed for 100 cycles, thereby indicating its mechanical robustness to repeated use, as is shown in figure 9b (i). Furthermore, when the human subject performed daily activities with the PGS attached for 2 h, the subject's motion was not interrupted or constrained by the PGS, owing to its ultra-lightweight (3.9 mg cm^{-2}) and high flexibility. After the PGS was detached from the skin, no irritation (e.g., skin rash) was observed from where it was attached, as can be seen in figure 9b (ii). Thus, the design allows the PGS to be easily attached and removed as necessary, which can be used as a disposable and low-cost skin-mountable device.

3.5. Hand motion monitoring

Figure 10a shows a representative ΔR time history of the PGS when the finger repeatedly bent to different pre-calibrated angles in a random manner so as to prevent biasing the results if bending was monotonically increased (figure 3a (ii-vi)). The inset of figure 10b is the PGS' response corresponding

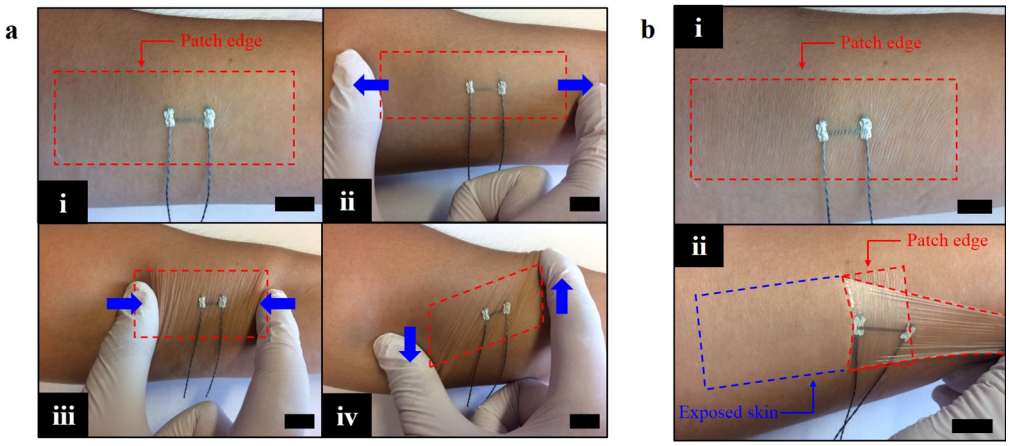

Figure 9. (a) Images of a PGS attached onto the skin in its (i) un-deformed state, followed by being subjected to (ii) compression, (iii) stretching, and (iv) shear. (b) (i) A PGS attached onto skin underwent 100 cycles of stretching/compressing. (ii) A PGS was peeled off and partially removed from the skin after being mounted for 2 h. The skin did not show any signs of sensitivity towards the tape and PGS. All scale bars, 20 mm.

to 15°-bending. In figure 11b, the average R_n and its standard deviations are plotted as a function of the corresponding bending angles. A least-squares regression line was fitted to the data in figure 10a, and an approximately linear sensor response can be observed. However, it can also be observed from figure 10b that some deviation to this linear response can be observed, particularly when bending increased from the initial straight state (0°) to 15°. This deviation could be a result of the low levels of strains applied when the finger was only bent to 15°.

Figure 11a (top) shows that the subject moved the (i) thumb, (ii) index, (iii) middle, (iv) ring, and (v) pinky fingers, individually, and then (vi) typing "UCSD" on the keyboard. Figure 11b (bottom) shows the corresponding R_n time history response of each sensing element in the PGS rosette, which indicates that different finger movements induced unique and complex strain patterns detectable by the rosette. The strain components (i.e., ε_x, ε_y, and shear γ_{xy}) were calculated based on the classical strain transformation equation [44]:

$$\varepsilon_i = \varepsilon_x \cos^2\theta_i + \varepsilon_y \sin^2\theta_i + \gamma_{xy}\sin\theta_i\cos\theta_i \qquad (i = a,b,c) \tag{2}$$

where θ_a, θ_b, and θ_c represent the angles from the ε_x-direction (i.e., where counterclockwise is positive to the S_a, S_b, and S_c directions), which are 135°, 90°, and 45°, respectively (figure 3b). In addition, the principal strains (i.e., maximum strain ε_1 and minimum ε_2) and principal direction (θ_1) were calculated as follows:

$$\varepsilon_{1,2} = \frac{\varepsilon_x + \varepsilon_y}{2} \pm \frac{1}{2}\sqrt{(\varepsilon_x - \varepsilon_y)^2 + \gamma^2_{xy}} \tag{3}$$

$$\theta_1 = \frac{1}{2}\tan^{-1}\left(\frac{\gamma_{xy}}{\varepsilon_x - \varepsilon_y}\right) \tag{4}$$

By assuming that strain varies linearly between sensing elements of the rosette, one can map the spatial strain distribution on the back of the hand using the strain transformation results obtained from the PGS rosette. In particular, figure 11b shows a schematic illustration for the derivation details. The dashed semicircle shows the sensing region of interest. $\vec{n}_0$ is the unit directional vector pointing to an arbitrary point (x_0,y_0), whereas $\vec{n}_x$ is projection of $\vec{n}_0$ onto the x-axis. The angle between $\vec{n}_x$ and $\vec{n}_0$ are denoted as θ_0. Then, the following can be obtained:

$$\vec{n}_x = (1,0); \vec{n}_0 = \frac{(x_0, y_0)}{\sqrt{x_0^2 + y_0^2}} \tag{5}$$

$$\cos\theta_0 = \vec{n}_x \cdot \vec{n}_0 = \frac{x_0}{\sqrt{x_0^2 + y_0^2}}; \sin\theta_0 = \vec{n}_x \times \vec{n}_0 = \frac{y_0}{\sqrt{x_0^2 + y_0^2}} \tag{6}$$

$$\varepsilon_0 = \varepsilon_x \cos^2\theta_0 + \varepsilon_y \sin^2\theta_0 + \gamma_{xy}\sin\theta_0\cos\theta_0 \tag{7}$$

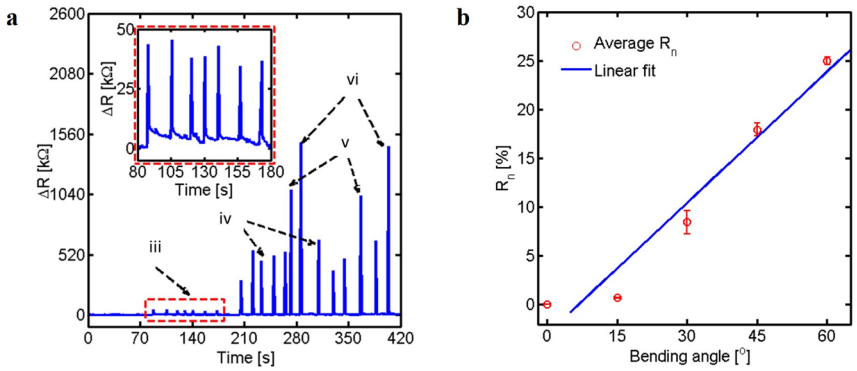

Figure 10. (a) The ΔR time history of the PGS corresponding to finger bending. The inset shows the ΔR due to the 15° finger bending case (highlighted in the dashed box). (b) The average R_n plotted as a function of bending angles (standard deviations as error bars), and fitted with a least-squares regression line.

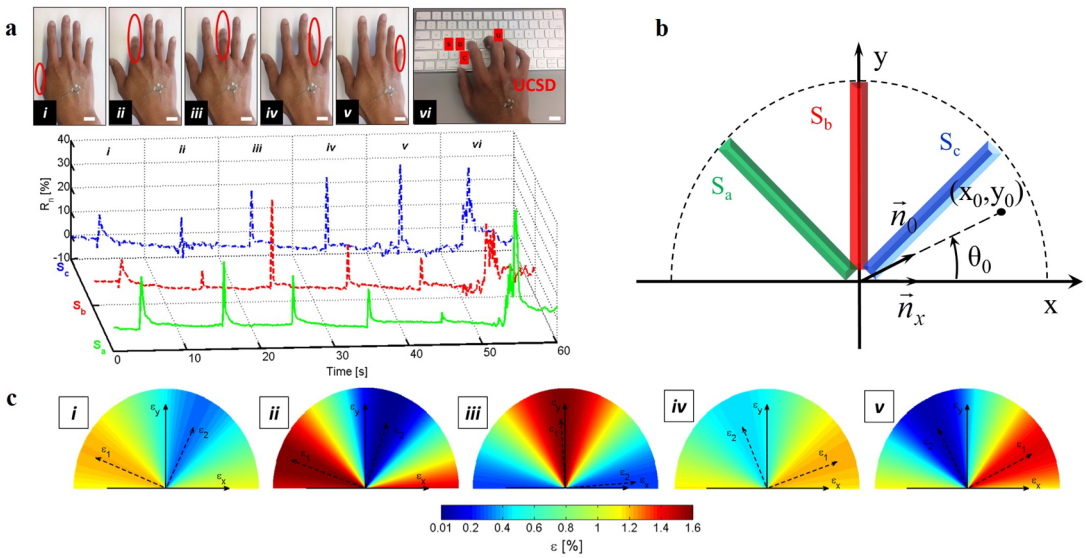

Figure 11. (a) (Top) Images of different finger and hand motion patterns (i.e., when the subjected moved the (i) thumb, (ii) index finger, (iii) middle finger, (iv) ring finger, and (v) pinky finger, followed by (vi) typing "UCSD"). (Bottom) The representative R_n time history of each sensing element of the PGS rosette corresponding to the different motions. All scale bars, 20 mm. (b) A schematic of mapping the complex 2D strain field. (c) Spatio-temporal maps of strain distribution induced by different hand motions in (a), as measured by the PGS rosette, overlaid with the computed principal strains (ε_1 and ε_2).

where ε_0 represents the strain at the arbitrary point. It was assumed that strain remains constant along each radial direction from the origin, and R_n was converted to strains using 21 as the GF ($\varepsilon = R_n/GF$). Strain mapping was performed using Matlab (MathWorks).

Figure 11c illustrates the spatio-temporal maps of strain distributions of the hand corresponding to different fingers moving. Figure 11c shows that the PGS successfully captured and distinguished the minor change in strain distribution on the hand due to contractions of different muscle groups when different fingers moved. Instead of implementing multiple sensors on each finger as reported previously [5, 45, 46], this study showed that a single PGS rosette can recognize the movements of the entire hand with high fidelity. The PGS can be beneficial for establishing new human-machine interfaces, as well as providing insightful information for human behavioral assessment and muscle-epidermis interactions.

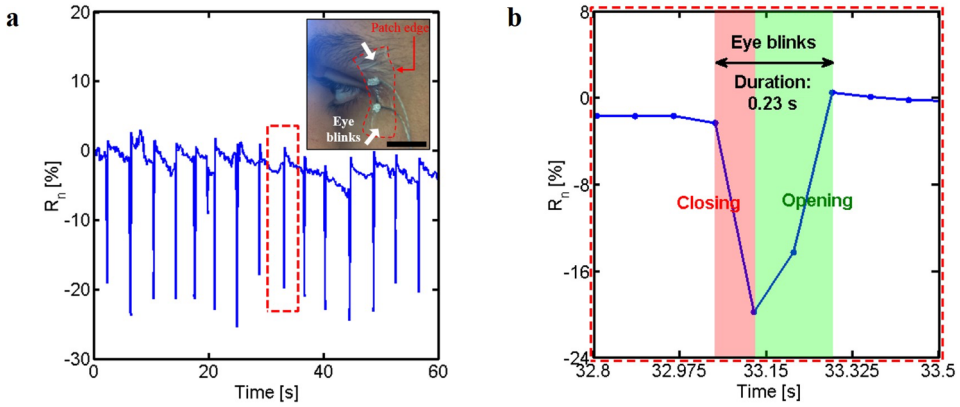

Figure 12. (a) The representative R_n time history of a PGS corresponding to eye blinking. The inset shows a PGS that was mounted on the subject' lateral canthus. (b) Detailed view of the R_n data included in the dashed box in (a).

3.6. Human physiological performance monitoring

First, the PGS was utilized to detect the eye blinking, as is depicted in the inset of Figure 12a. Figure 12a shows the R_n time history response of the PGS when the subject blinked repeatedly, where each drop in R_n indicates a blink. Here, the PGS' resistance decreased because the GNS sensing element was compressed in the vertical direction together with the lateral canthus when the eye closed. Figure 12b shows a representative detailed view of the change in R_n during an eye blink (i.e., corresponding to the region highlighted in figure 12a). The results confirmed that eye closing and opening corresponded to the drop and increase in R_n, respectively. In addition, the form factor of the PGS enabled it to capture the transient blinking process in a reversible manner without restricting eye motions or causing user discomfort.

Furthermore, the PGS' capability for monitoring pulsation was studied, as is shown in the inset of figure 13a. Figure 13a shows the pulse signal measured by the PGS when the subject was at rest and after rigorous exercise. The PGS exhibited good SNR due to its high strain sensitivity and conformability. Figure 13b provides a detailed view of the cardiac cycles highlighted in Figure 13a. The typical features of a radial pulse wave (including systolic peak, diastolic peak, and dicrotic notch) are distinguishable from the sensor's measurements when the subject was at rest [32, 47, 48]. The time interval between the systolic and diastolic peaks (ΔT) was measured as ~ 310 ms, which was normal for adults in their twenties [47]. It is known that ΔT depends on artery stiffness, which increases with age. Artery stiffness is a precursor for various cardiovascular diseases, such as myocardial infarction and stroke [49]. To further quantify artery stiffness, stiffness index (SI) can be calculated as follows [47,

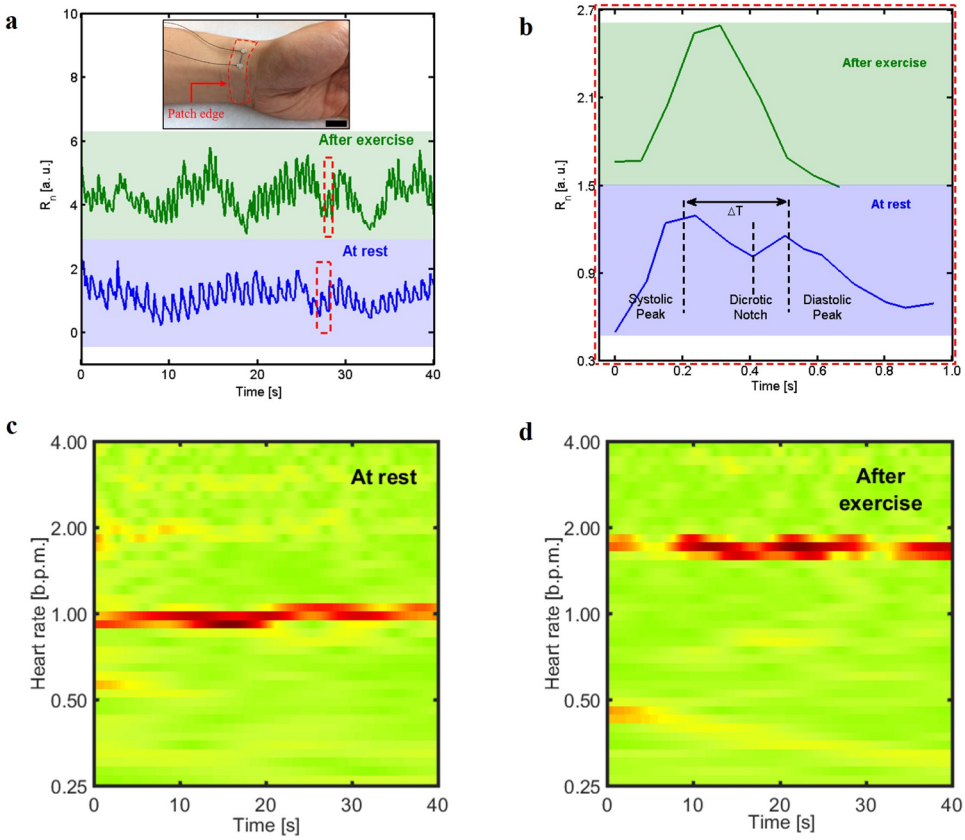

Figure 13. (a) The representative R_n time history of the PGS when it was employed for monitoring radial pulse of a human subject at rest and after exercise. The inset shows the sensor attached to the wrist of the subject. R_n is of arbitrary unit for easy comparison. Scale bar, 20 mm. (b) The radial pulse waveforms in the dashed boxes in (a). (c, d) Heart rate spectrograms when the subject was at rest and after exercise, respectively. The red regions indicate the dominant frequencies (i.e., measured heart rates).

48]:

$$SI = \frac{H}{\Delta T} \tag{8}$$

where H is the height of the human subject. Here, SI was calculated to be ~ 5.6 m s^{-1}, which is within the normal range for a healthy adult [47, 48]. However, the measured radial pulse waveform could not distinguish the aforementioned features after the subject exercised (figure 13b) [32].

In addition, to quantify heart rate, the radial pulse signals were analyzed using continuous wavelet transform (CWT), thereby enabling time and frequency localization. Figure 13c and 14d show the real-time heart rate spectrograms when the subject was at rest and after exercise, respectively. The red regions represent dominant frequencies of the radial pulse signals, which were converted to heart rates. The average heart rates of the subject at rest and after exercise were 60 beat per minute (bpm) and 114 bpm, respectively, which were both within the normal range.

4. Conclusion

In summary, this paper presented a graphene-based, skin-like, wearable sensor for human motion and physiological monitoring. In this study, few-layered and structurally intact GNS were synthesized using an optimized WALPE method so as to preserve their extraordinary electrical and mechanical. To harness the superior properties of GNS, a micro-patterning technique was employed to precisely and effectively fabricate GNS-based strain sensing elements of different geometries. The designed PGS was highly flexible, ultra-lightweight, conformable, and could be easily adhered or detached from the skin. In addition, it was also characterized by a high bilinear strain sensitivity with high signal-to-noise ratio, repeatability, and mechanical robustness. Furthermore, this study investigated its applications for human monitoring by attaching the PGS to different parts of the human body. The experiments validated that the PGS was able to quantify finger bending, identify hand motion patterns (and strain distributions), monitor eye blinking, and evaluate radial pulse signals. To improve the practical applicability of PGS, future work will focus on incorporating flexible wireless transmission circuits. In addition, by further employing the versatile and low-cost printing technique, more complex sensor designs with multi-modal sensing capabilities can be realized. The vision is that PGS can potentially be used as a low-cost, disposable, wearable device for human-machine interfaces, rehabilitation, human performance assessment, and even telemedicine.

Acknowledgements

This research was supported by the U.S. Office of Naval Research under contract no. N00014-17-1-2668 (principal investigator: Prof. Loh) and the Ministry of Science and Technology (MOST) of Taiwan (MOST Grant no. MOST 104-2923-E-011-001-MY3 and MOST 105-2221-E-011-141) (principal investigator: Prof. Chiang).

References

[1] Yeo J C, Lim C T 2016 Emerging flexible and wearable physical sensing platforms for healthcare and biomedical applications *Microsystems & Nanoengineering* **2**

[2] Yamada T, Hayamizu Y, Yamamoto Y, Yomogida Y, Izadi-Najafabadi A, Futaba D N, Hata K 2011 A stretchable carbon nanotube strain sensor for human-motion detection *Nature nanotechnology* **6** 296-301

[3] Kim D-H, Lu N, Ma R, Kim Y-S, Kim R-H, Wang S, Wu J, Won S M, Tao H, Islam A 2011 Epidermal electronics *science* **333** 838-843

[4] Xiao X, Yuan L, Zhong J, Ding T, Liu Y, Cai Z, Rong Y, Han H, Zhou J, Wang Z L 2011 High-Strain Sensors Based on ZnO Nanowire/Polystyrene Hybridized Flexible Films *Advanced materials* **23** 5440-5444

[5] Amjadi M, Pichitpajongkit A, Lee S, Ryu S, Park I 2014 Highly stretchable and sensitive strain sensor based on silver nanowire–elastomer nanocomposite *ACS nano* **8** 5154-5163

[6] Guo X, Huang Y, Cai X, Liu C, Liu P 2016 Capacitive wearable tactile sensor based on smart textile substrate with carbon black/silicone rubber composite dielectric *Measurement Science and Technology* **27** 045105

[7] Xiaohui G, Ying H, Can W, Leidong M, Yue W, Zhicheng X, Caixia L, Yugang Z 2017 Flexible and reversibly deformable radio-frequency antenna based on stretchable SWCNTs/PANI/Lycra conductive fabric *Smart Materials and Structures* **26** 105036
[8] Cheng Y, Wang R, Sun J, Gao L 2015 A Stretchable and Highly Sensitive Graphene-Based Fiber for Sensing Tensile Strain, Bending, and Torsion *Advanced materials* **27** 7365-7371
[9] Zeng W, Shu L, Li Q, Chen S, Wang F, Tao X M 2014 Fiber-based wearable electronics: a review of materials, fabrication, devices, and applications *Advanced materials* **26** 5310-5336
[10] Li Y-Q, Zhu W-B, Yu X-G, Huang P, Fu S-Y, Hu N, Liao K 2016 Multifunctional Wearable Device Based on Flexible and Conductive Carbon Sponge/Polydimethylsiloxane Composite *ACS Applied Materials & Interfaces* **8** 33189-33196
[11] Ryu S, Lee P, Chou J B, Xu R, Zhao R, Hart A J, Kim S-G 2015 Extremely elastic wearable carbon nanotube fiber strain sensor for monitoring of human motion *ACS nano* **9** 5929-5936
[12] Shi J, Li X, Cheng H, Liu Z, Zhao L, Yang T, Dai Z, Cheng Z, Shi E, Yang L 2016 Graphene reinforced carbon nanotube networks for wearable strain sensors *Advanced Functional Materials* **26** 2078-2084
[13] Wang Y, Wang L, Yang T, Li X, Zang X, Zhu M, Wang K, Wu D, Zhu H 2014 Wearable and highly sensitive graphene strain sensors for human motion monitoring *Advanced Functional Materials* **24** 4666-4670
[14] Bae S-H, Lee Y, Sharma B K, Lee H-J, Kim J-H, Ahn J-H 2013 Graphene-based transparent strain sensor *Carbon* **51** 236-242
[15] Choi M K, Park I, Kim D C, Joh E, Park O K, Kim J, Kim M, Choi C, Yang J, Cho K W 2015 Thermally controlled, patterned graphene transfer printing for transparent and wearable electronic/optoelectronic system *Advanced Functional Materials* **25** 7109-7118
[16] Tao L-Q, Zhang K-N, Tian H, Liu Y, Wang D-Y, Chen Y-Q, Yang Y, Ren T-L 2017 Graphene-Paper Pressure Sensor for Detecting Human Motions *ACS nano*
[17] Kim J, Lee M, Shim H J, Ghaffari R, Cho H R, Son D, Jung Y H, Soh M, Choi C, Jung S 2014 Stretchable silicon nanoribbon electronics for skin prosthesis *Nature communications* **5** 5747
[18] Imani S, Bandodkar A J, Mohan A V, Kumar R, Yu S, Wang J, Mercier P P 2016 A wearable chemical–electrophysiological hybrid biosensing system for real-time health and fitness monitoring *Nature communications* **7** ncomms11650
[19] Shin K Y, Hong J Y, Jang J 2011 Micropatterning of Graphene Sheets by Inkjet Printing and Its Wideband Dipole-Antenna Application *Advanced materials* **23** 2113-2118
[20] Finn D J, Lotya M, Cunningham G, Smith R J, McCloskey D, Donegan J F, Coleman J N 2014 Inkjet deposition of liquid-exfoliated graphene and MoS 2 nanosheets for printed device applications *Journal of Materials Chemistry C* **2** 925-932
[21] Li J, Ye F, Vaziri S, Muhammed M, Lemme M C, Östling M 2013 Efficient inkjet printing of graphene *Advanced materials* **25** 3985-3992
[22] Manna K, Hsieh C-Y, Lo S-C, Li Y-S, Huang H-N, Chiang W-H 2016 Graphene and graphene-analogue nanosheets produced by efficient water-assisted liquid exfoliation of layered materials *Carbon* **105** 551-555
[23] Manna K, Huang H-N, Li W-T, Ho Y-H, Chiang W-H 2016 Toward Understanding the Efficient Exfoliation of Layered Materials by Water-Assisted Cosolvent Liquid-Phase Exfoliation *Chemistry of materials* **28** 7586-7593
[24] Larson B J, Gillmor S D, Lagally M G 2004 Controlled deposition of picoliter amounts of fluid using an ultrasonically driven micropipette *Review of Scientific Instruments* **75** 832-836
[25] Tchvialeva L, Zeng H, Markhvida I, McLean D I, Lui H, Lee T K, "Skin roughness assessment," in *New Developments in Biomedical Engineering*, ed: InTech, 2010.
[26] Jeong J W, Yeo W H, Akhtar A, Norton J J, Kwack Y J, Li S, Jung S Y, Su Y, Lee W, Xia J 2013 Materials and Optimized Designs for Human-Machine Interfaces Via Epidermal Electronics *Advanced materials* **25** 6839-6846
[27] Pang C, Koo J H, Nguyen A, Caves J M, Kim M G, Chortos A, Kim K, Wang P J, Tok J B H, Bao Z 2015 Highly Skin-Conformal Microhairy Sensor for Pulse Signal Amplification *Advanced materials* **27** 634-640
[28] Drotlef D M, Amjadi M, Yunusa M, Sitti M 2017 Bioinspired Composite Microfibers for Skin Adhesion and Signal Amplification of Wearable Sensors *Advanced materials*

[29] Majerus S, Gill-Thwaites H, Andrews K, Laureys S 2005 Behavioral evaluation of consciousness in severe brain damage *Progress in brain research* **150** 397-413
[30] León-Carrión J, Eeckhout P v, Domínguez-Morales M d R 2002 Review of subject: the locked-in syndrome: a syndrome looking for a therapy *Brain injury* **16** 555-569
[31] Richard I, Pereon Y, Guiheneu P, Nogues B 1995 Persistence of distal motor control in the locked in syndrome. Review of 11 patients I Richard!, Y Pereon2, P Guiheneu2, B Nogues2, B Perrouin-Verbe1 and JF Mathe1 *Paraplegia* **33** 640-646
[32] Avolio A P, Butlin M, Walsh A 2009 Arterial blood pressure measurement and pulse wave analysis—their role in enhancing cardiovascular assessment *Physiological Measurement* **31** R1
[33] Lee C, Yan H, Brus L E, Heinz T F, Hone J, Ryu S 2010 Anomalous lattice vibrations of single- and few-layer MoS2 *ACS nano* **4** 2695-2700
[34] Eckmann A, Felten A, Mishchenko A, Britnell L, Krupke R, Novoselov K S, Casiraghi C 2012 Probing the nature of defects in graphene by Raman spectroscopy *Nano Letters* **12** 3925-3930
[35] Bracamonte M, Lacconi G, Urreta S, Foa Torres L 2014 On the nature of defects in liquid-phase exfoliated graphene *The Journal of Physical Chemistry C* **118** 15455-15459
[36] Hernandez Y, Nicolosi V, Lotya M, Blighe F M, Sun Z, De S, McGovern I, Holland B, Byrne M, Gun'Ko Y K 2008 High-yield production of graphene by liquid-phase exfoliation of graphite *Nature nanotechnology* **3** 563-568
[37] Smith A, Niklaus F, Paussa A, Vaziri S, Fischer A C, Sterner M, Forsberg F, Delin A, Esseni D, Palestri P 2013 Electromechanical piezoresistive sensing in suspended graphene membranes *Nano Letters* **13** 3237-3242
[38] Zhu S-E, Krishna Ghatkesar M, Zhang C, Janssen G 2013 Graphene based piezoresistive pressure sensor *Applied Physics Letters* **102** 161904
[39] Lee B M, Loh K J, Yang Y-S 2017 Carbon nanotube thin film strain sensor models assembled using nano- and micro-scale imaging *Computational Mechanics* **60** 39-49
[40] Wang L, Loh K J, Brely L, Bosia F, Pugno N M 2016 An experimental and numerical study on the mechanical properties of carbon nanotube-latex thin films *Journal of the European Ceramic Society* **36** 2255-2262
[41] Yeo W H, Kim Y S, Lee J, Ameen A, Shi L, Li M, Wang S, Ma R, Jin S H, Kang Z 2013 Multifunctional epidermal electronics printed directly onto the skin *Advanced materials* **25** 2773-2778
[42] Amjadi M, Kyung K U, Park I, Sitti M 2016 Stretchable, Skin-Mountable, and Wearable Strain Sensors and Their Potential Applications: A Review *Advanced Functional Materials* **26** 1678-1698
[43] Li X, Zhang R, Yu W, Wang K, Wei J, Wu D, Cao A, Li Z, Cheng Y, Zheng Q 2012 Stretchable and highly sensitive graphene-on-polymer strain sensors *Scientific reports* **2** 870
[44] E. M G 1969 *Schaum's Outline of Continuum Mechanics*McGraw-Hill
[45] Gong S, Lai D T, Wang Y, Yap L W, Si K J, Shi Q, Jason N N, Sridhar T, Uddin H, Cheng W 2015 Tattoolike polyaniline microparticle-doped gold nanowire patches as highly durable wearable sensors *ACS Applied Materials & Interfaces* **7** 19700-19708
[46] Lee J, Kim S, Lee J, Yang D, Park B C, Ryu S, Park I 2014 A stretchable strain sensor based on a metal nanoparticle thin film for human motion detection *Nanoscale* **6** 11932-11939
[47] Elgendi M 2012 On the analysis of fingertip photoplethysmogram signals *Current cardiology reviews* **8** 14-25
[48] Fan Z, Zhang G, Liao S 2009 *Clinical analysis for cardiovascular disease by calculating Stiffness Index, Cardiac Output from pulse wave* Electrical and Computer Engineering, 2009. CCECE'09. Canadian Conference on
[49] Moon S-H, Moon J-C, Heo D-H, Lim Y-H, Choi J-H, Kim S-Y, Kim K-S, Joo S-J 2015 Increased pulse wave velocity and augmentation index after isometric handgrip exercise in patients with coronary artery disease *Clinical hypertension* **21** 5